Evaluation of Sugar Content and Yield in Sugar Beet Based on UAV Multi-Sensor

Yeying Zhou and Yuntao Ma

Abstract—**Sugar beet is a major sugar crop in temperate regions and rapid, high-throughput, and accurate estimation of field phenotypes is essential for variety selection and production optimization. In this paper, ten commercial sugar beet varieties adapted to high latitudes are investigated using unmanned aerial vehicle (UAV) based red-green-blue (RGB), multispectral, and thermal infrared imaging across multiple growth stages. Canopy structural, texture, spectral, and temperature features are extracted, and three machine learning algorithms, random forest (RF), partial least squares (PLS), and support vector machine (SVM), are used to predict sugar content, root fresh weight, and yield. The results show that all three methods estimate sugar content well, with relative root mean square error (rRMSE) values below 11.0%, while RF and PLS outperform SVM. Multispectral features provide higher accuracy than RGB features, and multi-sensor feature combinations generally improve sugar content prediction compared with single-sensor inputs. For root fresh weight, SVM slightly outperforms RF and PLS, and RGB features are more informative than multispectral features. The integration of thermal infrared features does not notably improve RF or PLS models, but the combination of multispectral and thermal infrared features achieves the best SVM performance ($R^2 = 0.58$, RMSE = 75.3 g, and rRMSE = 23.7%). For yield estimation, RF achieves the highest accuracy, with rRMSE values ranging from 15.4% to 18.8%. Yield prediction accuracy increases as the time of image acquisition approaches harvest, and combining multi-temporal data from periods close to harvest further improves model performance. Overall, multi-sensor UAV data can effectively estimate sugar content, root fresh weight, and yield in sugar beet, providing a useful approach for phenotypic analysis, precision management, and variety selection.**

Index Terms—**Data fusion, plant phenotype, multi-source data, machine learning**

I. Introduction

SUGAR beet is one of the major sugar crops and an important economic crop in many countries [1, 2]. With global population growth and rising living standards, the demand for sugar continues to increase. Therefore, the selection of sugar beet varieties with strong adaptability, high yield, and superior quality has become increasingly important for addressing challenges such as rapid climate change and limited land resources [3]. The key traits, including plant height, sugar content, root fresh weight, and yield, are important indicators for both farm management and varietal evaluation, as they provide essential information for regulating crop growth and identifying superior genotypes [4]. With the expansion of large-scale mechanized sugar beet production, rapid, accurate, and multi-temporal monitoring of crop growth has become increasingly important for supporting production management and decision-making.

In recent years, sugar beet production has gradually transitioned from manual cultivation to mechanized management, with multifunctional agricultural machinery playing a key role in the modern production systems. Meanwhile, advances in remote sensing have provided rapid, non-destructive, and efficient tools for crop growth monitoring [5, 6]. Agricultural remote sensing platforms mainly include ground-based systems, unmanned aerial vehicles (UAVs), and satellites [7]. Ground-based measurements are labor-intensive, may disturb crop canopies during data collection, and are generally unsuitable for acquiring orthorectified field-scale imagery [8]. Satellite remote sensing enables non-invasive and large-scale crop monitoring, but its utility is often limited by long revisit intervals and weather-related constraints, particularly cloud cover, which can compromise the timeliness and accuracy of crop assessment and yield prediction [9, 10]. Compared with these platforms, UAVs provide greater flexibility, higher spatial resolution, and lower field interference, making them particularly suitable for high-throughput phenotyping and precision agricultural applications [11, 12].

UAV platforms can be equipped with a variety of sensors, including red-green-blue (RGB), multispectral, hyperspectral, thermal infrared, and light detection and ranging (LiDAR) sensors [13]. Among these, RGB sensors are the most widely used in UAV-based crop phenotyping because of their low cost and high spatial resolution. However, their spectral information is limited to the visible red, green, and blue bands. Even so, UAV-based RGB imagery has been widely applied to extract crop phenotypic traits such as plant height [14], emergence rate [15], plant density [16], biomass [17], leaf area [18], and canopy coverage [19]. Compared with RGB sensors, multispectral sensors provide additional reflectance information in the red-edge and near-infrared bands, which is useful for constructing vegetation indices sensitive to crop physiological and biochemical status. These features have been widely used to estimate nitrogen content [20], chlorophyll content [21], disease occurrence [22], biomass [23], and other physiological traits. Thermal infrared sensors, by

Manuscript received: 14 February 2026; revised: 12 March 2026; accepted: 15 March 2026. *(Corresponding author: Yuntao Ma.)*

Citation: Y. Zhou and Y. Ma, Evaluation of sugar content and yield in sugar beet based on UAV multi-sensor, *Int. J. Intell. Control Syst.*, 2026, 31(1), 72–84.

Yeying Zhou is with Biotechnology Research Institute, Inner Mongolia Academy of Science and Technology, Hohhot 010010, China, and also with College of Land Science and Technology, China Agricultural University, Beijing 100093, China (e-mail: yeying@agro.au.dk).

Yuntao Ma is with College of Land Science and Technology, China Agricultural University, Beijing 100093, China (e-mail: yuntao.ma@cau.edu.cn).

Digital Object Identifier 10.62678/IJICS202603.10313

contrast, capture surface temperature information through thermal radiation and are particularly valuable for assessing crop responses to environmental stress. UAV-based thermal imagery has been used to monitor crop water content [24], water stress [25], and canopy temperature differences related to the crop condition [26].

Recent studies have shown that combining canopy spectral, structural, thermal, and textural information from different sensor systems can improve the estimation of plant traits in a wide range of agricultural applications. For example, Liu et al. [26] quantified rice lodging status using texture features, such as roughness, contrast, linear patterns, and orientation, extracted from UAV imagery. Maimaitijiang et al. [27] improved soybean yield prediction by integrating UAV-derived spectral data, canopy structural information, and thermal imagery. These studies highlight the value of multi-source UAV data for improving crop trait estimation. Given the high economic importance and broad utilization value of sugar beet, the use of advanced UAV-based high-throughput phenotyping and multi-source image analysis is of great significance for growth monitoring and production support. Previous studies have demonstrated the potential of UAV remote sensing in sugar beet research. For instance, Khoshboresh-Masouleh et al. [28] improved the segmentation of sugar beet and weeds from multispectral UAV imagery using deep learning methods. Wang et al. [29] also quantified sugar content in sugar beet using UAV-based RGB imagery and LiDAR data to compare internal point cloud distribution and reconstruct the three-dimensional canopy structure. However, among these studies, UAV-based applications in sugar beet have mainly focused on nutrient diagnosis, weed detection, disease monitoring, and chlorophyll-related traits. In contrast, the combined use of canopy spectral and structural information for predicting the key sugar beet physiological and yield-related traits remains relatively limited. This gap highlights the need for further research on multi-source UAV data integration for comprehensive sugar beet phenotyping and trait estimation.

This paper aims to predict sugar content, root fresh weight, and yield in sugar beet using multi-source UAV data. The specific objectives are to: (1) assess the potential of multi-sensor UAV data for predicting these key traits; (2) compare the performance of different machine learning methods; and (3) quantify the contributions of structural, textural, spectral, and thermal features to trait prediction.

II. Materials and Methods

A. Experimental Setup

The field experiment is conducted at Suqin Agricultural Pasture, Sanhe Huimin Township, Hulunbuir, Inner Mongolia Autonomous Region, China (119°53′1″ E, 50°28′56″ N). The study area is characterized by a mid-temperate continental steppe climate, with a mean annual temperature ranging from −5 to 3 °C, average annual precipitation of 358.6 mm, annual sunshine duration of 2500–3000 h, and a frost-free period of approximately 89 days. Ten commercial sugar beet varieties with high agronomic potential (MK4044, MK4085, LN17101-1805, SV1588, KN1387, KUHN1357, KW2314, LN17101-1210, LN17101, and SR411) are used as experimental materials. Sugar beet was sown on 20 May 2021. Each variety is planted in three replicate plots, resulting in a total of 30 plots. Each plot consisted of three rows, with a row spacing of 50.0 cm and a plant spacing of 20.0 cm. The distance between adjacent plots is 0.5 m, and field management practices are kept consistent across all plots. The layout of the experimental plots is shown in Fig. 1.

B. Data Collection and Processing

(1) Field data collection. Field data are collected at five time points covering two key growth stages of sugar, as shown in Table 1. The measured variables include canopy temperature, plant height, root fresh weight, and sugar content. Temperature calibration is performed using handheld infrared thermometers (FLUKE62MAX+ and FT-F41) and the average of three measurements is taken as the reference temperature of the calibration plate. In each plot, three sugar beet plants are randomly selected and plant height is determined as the vertical distance from the highest point of the canopy to the ground. The mean of the three measurements is used as the observed plant height for that plot. Root fresh weight and sugar content are determined based on the three sampled plants and then scaled according to planting density to obtain plot-level values. The sugar content of the sampled beet roots is measured using a handheld sugar meter (PAL-1, Japan) and the average value of the three samples is taken as the observed sugar content of the plot. The equations used to calculate sugar content and yield are presented in Eqs. (1) and (2), respectively.

$$\mathrm{SY} = \mu \times \mathrm{RFW} \times \mathrm{SC} \quad (1)$$

where SY is the sugar content of sugar beet, RFW is the mean fresh weight of the beet root, SC is the measured sugar

Table 1 Sampling schedule.

Sampling period	Days after sowing	Sensor	Measurement indicator
5 July 2021, rapid leaf clump growth period	47	Digital	Plant height and biomass
21 July 2021, early stages of tuber sugar growth	63	Digital	Plant height, biomass, and sugar content
30 July 2021, medium-term stages of tuber sugar growth	72	Digital, multispectral, and thermal infrared	Plant height, biomass, sugar content, and temperature
13 August 2021, late stages of tuber sugar growth	86	Digital, multispectral, and thermal infrared	Plant height, biomass, sugar content, and temperature
21 August 2021, early stages of sugar accumulation	94	Digital, multispectral, and thermal infrared	Plant height, biomass, sugar content, and temperature
20 September 2021, harvesting period	124	—	Biomass and sugar content

content of the beetroot tuber, and μ is the empirical coefficient, $\mu = 0.85$.

$$Y = \text{RFW} \times S \times N \tag{2}$$

where Y is the yield of sugar beet, N is the emergence rate, and S is the planting density of sugar beet. $N = 0.7948$, $S = 10$ plants/m^2, and $Y = 7.948 \times \text{RFW}$ kg/m^2.

(2) Digital images from the UAV platform. The RGB images of the study area are acquired using a DJI Phantom 4 RTK UAV (DJI, Shenzhen, China), which has a flight time of approximately 30 min and is equipped with a 20 megapixel camera, as shown in Fig. 1. Thermal infrared images are collected using a DJI Matrice 200 V2 UAV (DJI, Shenzhen, China) equipped with a Zenmuse XT2 thermal infrared sensor (DJI, Shenzhen, China), as shown in Fig. 2. This platform has a flight time of approximately 38 min and a loaded flight time of about 24 min. Multispectral images are acquired using a DJI Inspire 2 UAV (DJI, Shenzhen, China) equipped with a RedEdge-M five-band multispectral camera (MicaSense, Seattle, WA, USA), as shown in Fig. 2. The five spectral bands include blue (475 nm center wavelength and 20 nm bandwidth), green (560 nm center wavelength and 20 nm bandwidth), red (668 nm center wavelength and 10 nm bandwidth), red edge (717 nm center wavelength and 10 nm bandwidth), and near-infrared (840 nm center wavelength and 40 nm bandwidth).

The acquisition dates for the RGB, thermal infrared, and multispectral images are listed in Table 1, and ground measurements are collected on the same days. Flight missions are planned using DJI Pilot software. The flight altitude is set to 30.0 m, with front and side overlap of 80% for RGB imagery and 90% for thermal infrared and multispectral imagery. The spatial resolutions of the RGB, thermal infrared, and multispectral images are 0.83, 2.84, and 2.18 cm/pixel, respectively. All flights are conducted under clear and calm weather conditions between 11:00 and 14:00. Four ground control points (GCPs) are evenly distributed across the experimental field. The longitude, latitude, and elevation of each GCP are measured using a real-time kinematic (RTK) system (Huazheng, Shanghai, China) to determine the three-dimensional coordinates of the center point of each marker.

Metashape Pro v1.7.1 (Agisoft, St. Petersburg, Russia) is used for RGB image alignment and mosaicking. Geometric correction and georeferencing are performed using the geographic coordinates of the GCPs to optimize image alignment. Based on the built-in structure-from-motion (SfM) algorithm, a dense three-dimensional point cloud, a digital surface model (DSM), and the digital orthomosaic (DOM) are generated for the entire study area. The spatial resolutions of the DSM and DOM are 8.29 mm/pixel and 3.32 cm/pixel, respectively. Pix4Dmapper software (Pix4D SA, Lausanne, Switzerland) is used for radiometric calibration and mosaicking of the multispectral and thermal infrared images. Orthomosaic reflectance maps for each multispectral band are generated and vegetation indices are calculated accordingly. In addition, three-dimensional reflectance point clouds are reconstructed using the SfM algorithm, while absolute temperature maps are derived from the thermal infrared imagery using the index calculator module.

C. Characteristic Information Extraction from UAV Images

(1) Canopy spectral characteristics. In crop spectroscopy studies, band reflectance can be used both to develop models for estimating physiological and biochemical traits and to

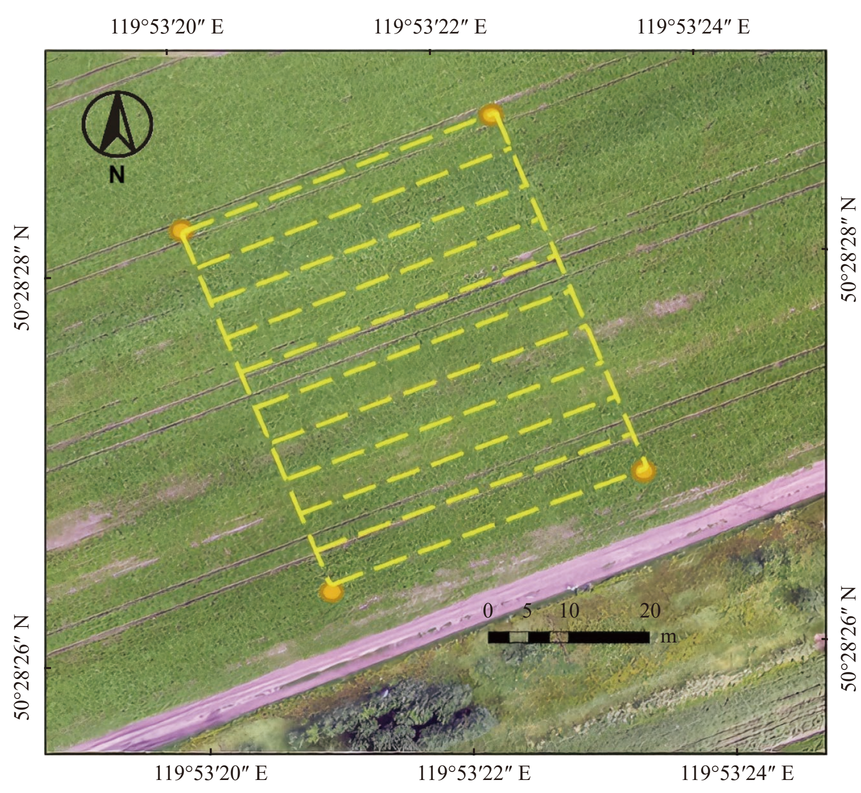

Fig. 1 Location of the study area and UAV orthophoto image acquired.

(a) DJI Phantom 4 RTK with CMOS (b) Matrice M200 V2 with Zenmuse XT2 (c) Inspire 2 with MicaSense RedEdge-M

Fig. 2 UAV and multi-sensor.

construct vegetation indices for assessing crop growth status. In this paper, commonly used vegetation indices are selected, as shown in Tables 2 and 3, and the normalized relative canopy temperature (NRCT) is derived from thermal infrared imagery as shown in Eq. (3). These indices can enhance specific crop signals while reducing the influence of external factors such as solar irradiance, canopy structure, and soil background.

$$\mathrm{NRCT} = \frac{T_i - T_{\min}}{T_{\max} - T_{\min}} \tag{3}$$

where T_i is the canopy temperature of the i-th pixel, $T_{\min}$ is the minimum temperature measured within the target area, and $T_{\max}$ is the maximum temperature measured within the target area, respectively.

To minimize the influence of soil background on the prediction of sugar content, root fresh weight, and yield in sugar beet, soil pixels are removed from the RGB, thermal infrared, and multispectral orthomosaics using threshold-based segmentation. For the RGB imagery, the color index of vegetation (CIVE) is used to separate vegetation from the background as shown in Eq. (4). The optimal threshold is determined from the frequency distribution of CIVE values, and the resulting binary image is used to generate a vegetation mask for soil removal. For the multispectral imagery, modified chlorophyll absorption ratio index (MCARI) is selected for image segmentation as shown in Eq. (5). Similarly, the optimal threshold is identified from the frequency distribution of modified chlorophyll absorption ratio index values to distinguish vegetation from the background pixels. For the thermal infrared imagery, because canopy temperature differs substantially from soil temperature at midday, the optimal threshold is determined from the frequency distribution of grayscale digital number values in the thermal images.

Table 2 Vegetation index calculation formula of RGB image extraction.

Vegetation index	Calculation formula	References
EXR	$1.4 \times r - g$	Meyer and Neto [30]
EXG	$2 \times g - r - b$	Woebbecke et al. [31]
EXGR	$3 \times g - 2.4 \times r$	Meyer and Neto [30]
GLI	$(2 \times g - b - r)/(2 \times g + b + r)$	Louhaichi et al. [32]
NGBDI	$(g - b)/(g + b)$	Verrelst et al. [33]
RGBVI	$(g^2 - b \times r)/((g^2 + b \times r)$	Bendig et al. [14]
VARI	$(g - r)/(g - b + r)$	Gitelson et al. [34]
VEG	$g/(r^k b^{1-k})$, $k = 0.667$	Woebbecke et al. [31]
WI	$(g - b)/(r - g)$	Woebbecke et al. [31]

Note: b, g, and r are bands of blue, green, and red reflectance, respectively.

Table 3 Multispectral vegetation index calculation extraction.

Vegetation index	Calculation formula	References
DVI	$1.4 \times \mathrm{nir} - r$	Tucker [35]
GNDVI	$(\mathrm{nir} - g)/(\mathrm{nir} + g)$	Gitelson and Merzlyak [36]
GRVI	$(g - r)/(g + r)$	Hague et al. [37]
MCARI	$((\mathrm{reg} - r) - 0.2 \times (\mathrm{reg} - g)) \times (\mathrm{reg}/r)$	Daughtry et al. [38]
MNVI	$(1.5 \times (\mathrm{nir}^2 - r))/(\mathrm{nir}^2 + r + 0.5)$	Gong et al. [39]
MSR	$(\mathrm{nir}/r - 1)/(\sqrt{\mathrm{nir}/r} + 1)$	Chen [40]
NDVI	$(\mathrm{nir} - r)/(\mathrm{nir} + r)$	Rouse [41]
NLI	$(\mathrm{nir}^2 - r)/(\mathrm{nir}^2 + r)$	Goel and Qin [42]
PPR	$(g - b)/(g + b)$	Metternicht [43]
RVI1	nir/r	Pearson and Miller [44]
RVI2	nir/g	Xue et al. [45]
TVI	$60 \times (\mathrm{nir} - g) - 100 \times (r - g)$	Broge and Leblanc [46]

Note: b, g, r, nir, and reg are bands of blue, green, red, near infrared, and red edge reflectance, respectively.

$$\mathrm{CIVE} = 0.441 \times R - 0.881 \times G + 0.385 \times B + 18.78745 \tag{4}$$

$$\mathrm{MCARI} = ((\mathrm{reg} - r) - 0.2 \times (\mathrm{reg} - g)) \times (\mathrm{reg}/r) \tag{5}$$

where R, G, and B are the red, green, and blue bands of RGB image, respectively. r, g, and reg are the red, green, and red edge bands of the multispectral image, respectively.

(2) Canopy structural characteristics. RGB images acquired at the five time points are used to generate the DSMs, and plant height is estimated as the elevation difference between the upper canopy surface and the ground surface within each plot, as shown in Fig. 3. After removal of the soil background, the RGB images are converted to grayscale. The gray-level co-occurrence matrix (GLCM) is then calculated using the "scikit-image" library in Python to extract eight texture features as shown in Table 4. In addition, vegetation fraction (VF) is calculated to quantify sugar beet canopy cover, defined as the ratio of sugar beet canopy pixels to the total number of pixels within each plot as shown in Eq. (6).

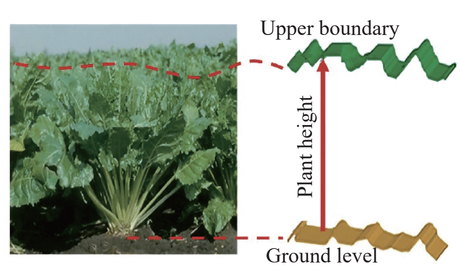

Fig. 3 Schematic diagram of plant height estimation.

$$\mathrm{VF} = \mathrm{PV}/(\mathrm{PA} \times N) \times 100 \tag{6}$$

where VF is the vegetation fraction, PA is the total number of pixels in the plot, PV is the number of vegetation pixels in the plot after the removal of soil, and N is the emergence rate.

D. Methodology

(1) Overview of the research process. This paper is based

Table 4 Texture characteristics.

Index	Abbreviation	Mathematical expression
Contrast	Con	$\sum_{i,j=0}^{N-1} P_{ij}(i-j)^2$
Correlation	Cor	$\sum_{i,j=0}^{N-1} P_{ij}\left[(i-\mu_i)(j-\mu_j)/\sqrt{(\sigma_i^2)(\sigma_j^2)}\right]$
Dissimilarity	Dis	$\sum_{i,j=0}^{N-1} P_{ij}(i-j)^2$
Energy	Ene	$\sum_{i,j=0}^{N-1} (P_{ij})^2(i-j)^2$
Entropy	Ent	$-\sum_{i,j=0}^{N-1} P_{ij}(\log P_{ij})$
Homogeneity	Hom	$\sum_{i,j=0}^{N-1} \log P_{ij}/1+(i-j)^2$
Mean	Mean	$\mu_i=\sum_{i,j=0}^{N-1} P_{ij}(P_{ij}),\ \mu_j=\sum_{i,j=0}^{N-1} P_{ij}(P_{ij})$

Note: i and j represent different pixel grey scale values.

on the multi-source UAV data collected at multiple time points during the root growth and sugar accumulation stages of sugar beet, including RGB, thermal infrared, and multispectral imagery. Structural, textural, thermal, and spectral features are extracted for variable selection. Machine learning algorithms, including random forest (RF), partial least squares regression (PLSR), and support vector machine (SVM), are then used to develop prediction models for sugar content, root fresh weight, and yield, and their predictive performance is evaluated. The optimal modelling methods and feature combinations for each trait are subsequently compared and analyzed. The overall workflow of the study is presented in Fig. 4.

(2) Variable selection. To reduce data dimensionality and eliminate variables with low predictive relevance, Pearson correlation analysis is applied for preliminary variable screening. The correlation coefficient is denoted by r and the closer $|r|$ is to 1, the stronger the correlation between variables. A positive r indicates a positive correlation, whereas a negative r indicates a negative correlation. In this paper, Pearson correlation coefficients are calculated between the target variables (yield, root fresh weight, and sugar content) and the extracted features, followed by significance testing. Only variables that are significantly correlated with the target variables at the $\alpha=0.01$ level are retained for further analysis to improve modelling efficiency and accuracy.

$$r=\frac{1}{N-1}\sum_{i=1}^{N}\left(\frac{X_i-\bar{X}}{S_X}\right)\left(\frac{Y_i-\bar{Y}}{S_Y}\right) \tag{7}$$

where N is the sample size, X_i, Y_i, $\bar{X}$, and $\bar{Y}$ are the observed and mean values of X and Y variables, and S_X and S_Y are the variance of X and Y variables, respectively.

To further reduce the set of variables, this paper uses the Boruta algorithm for secondary screening based on the results of correlation analysis. The Boruta algorithm is based on the RF model [47], which finds the optimal combination of characteristic variables [48]. The basic idea is to replicate the initial characteristic dataset, randomly disrupt the row order of each characteristic value to form a shadow characteristic, and then mix the initial characteristics with the shadow characteristics to form a new characteristic dataset. The importance score of each feature is obtained by applying multiple iterations of the random forest model. The resulting characteristic subset has the optimal combination of characteristics, which can minimize the error of the RF model.

In this paper, the Boruta algorithm is implemented in R package using the variables retained after Pearson correlation screening as input. The maximum number of iterations (maxRuns) is set to 100, which is the default setting commonly used in the Boruta package. Feature importance is evaluated iteratively by comparing the importance of the original variables with that of the shadow variables generated by random permutation. Variables classified as “confirmed” by the Boruta algorithm are retained for subsequent modelling, whereas variables classified as “rejected” are removed. Tentative variables are not included in the final modelling to ensure the robustness and interpretability of the selected feature set.

(3) Modelling and testing. Random forest regression (RFR), SVM, and PLSR are used to develop prediction

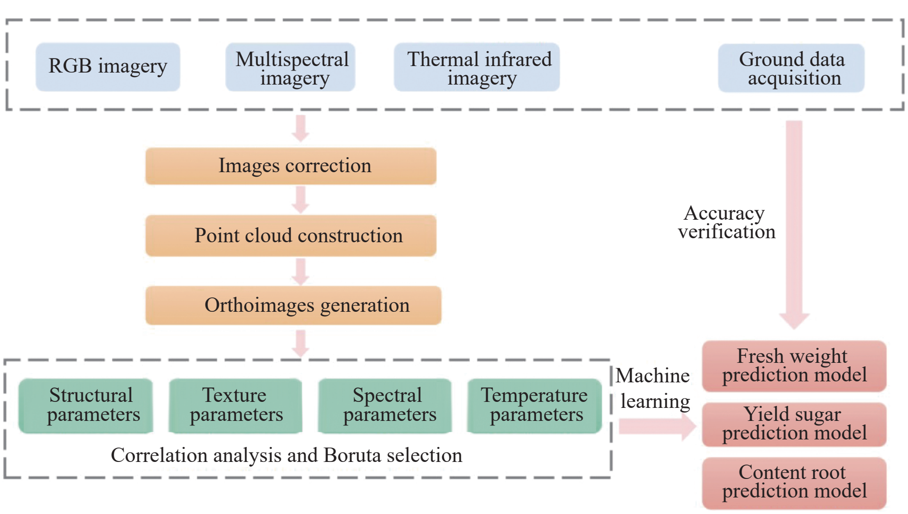

Fig. 4 Experimental processing flowchart.

models for sugar content, root fresh weight, and yield. To improve prediction performance, data from the three growth stages are combined for modelling. The features selected by the Boruta algorithm are used as inputs for the sugar content and root fresh weight models. For yield prediction, models are developed based on the feature set from the optimal sensor combination identified in the root fresh weight analysis, using either single-period features or combined features from multiple periods.

RFR is an ensemble learning method based on decision trees. Because each tree is trained using a bootstrap sample and a random subset of variables, RFR is relatively insensitive to multicollinearity and is well suited for high-dimensional data. This characteristic improves model robustness and helps reduce overfitting. In this paper, the number of trees (ntree) is set to 500 to ensure stable model performance, and the number of variables randomly selected at each split (mtry) is set to the default value defined by the R package according to the number of input variables.

PLSR is a multivariate modelling method that integrates multiple linear regression, principal component analysis, and canonical correlation analysis. Compared with conventional multiple linear regression, PLSR is more suitable when predictor variables are numerous and highly collinear and the sample size is limited. In this paper, the optimal number of latent variables is determined automatically by cross-validation using the default settings of the corresponding R package.

SVM maps the input data into a high-dimensional feature space through nonlinear transformation and identifies the optimal regression hyperplane by minimizing prediction error while maximizing the margin. This method performs well for nonlinear, small-sample, and high-dimensional problems. In this paper, the SVM model is implemented using the default radial basis function (RBF) kernel. The main parameters, including the cost parameter ($C = 1$) and the kernel parameter (γ), are set according to the default settings of the R package, with γ automatically determined based on the number of input variables.

The dataset is divided into training and testing sets at a ratio of 2:1. The coefficient of determination (R^2), root mean square error (RMSE), and relative root mean square error (rRMSE) are used to evaluate model performance. Higher R^2 values and lower RMSE and rRMSE values indicate better predictive accuracy.

III. Results

A. Results of the Screening of Characteristic Variables

(1) Correlation analysis of each phenotype with the characteristic parameters. Sugar content is significantly negatively correlated with RGB triple band reflectance and vegetation indices of GLI, NGBDI, RGBVI, and VEG, with $|r|$ ranging from 0.55 to 0.60. Root fresh weight is positively correlated with green band spectral reflectance, VARI and WI. It negatively correlated with GLI, NGBDI, RGBVI, and VEG, with $|r|$ ranging from 0.33 to 0.60, as shown in Fig. 5. The heat map color among all vegetation indices is dark and the correlation is high, indicating that the vegetation indices are purely strongly correlated with each other. It is necessary to further screen each phenotypically sensitive covariate using Boruta algorithm.

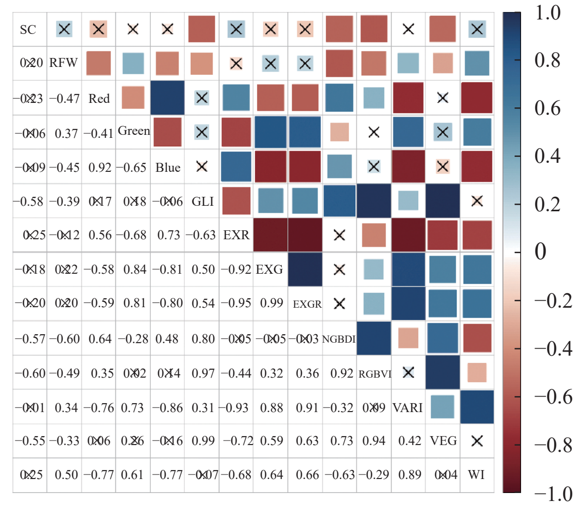

Fig. 5 Correlation analysis of RGB vegetation indices.

The sugar content is significantly positively correlated with four characteristic variables: coverage (VF), contrast (Con), heterogeneity (Dis), and variance (Var). The range of correlation coefficient r varies from 0.35 to 0.60. The sugar content is negatively correlated with Cor and Hom, with the range of r varying from −0.46 to −0.34. The root fresh weight is negatively correlated with three texture characteristics: Cor, Ene, and Hom, with the range of r varying from −0.61 to −0.40. The root fresh weight is positively correlated with VF, Con, Dis, Ent, Mean, and Var, with the range of r varying from 0.46 to 0.63, as shown in Fig. 6. There are significant correlations among eight texture characteristics, indicating a strong covariance between them.

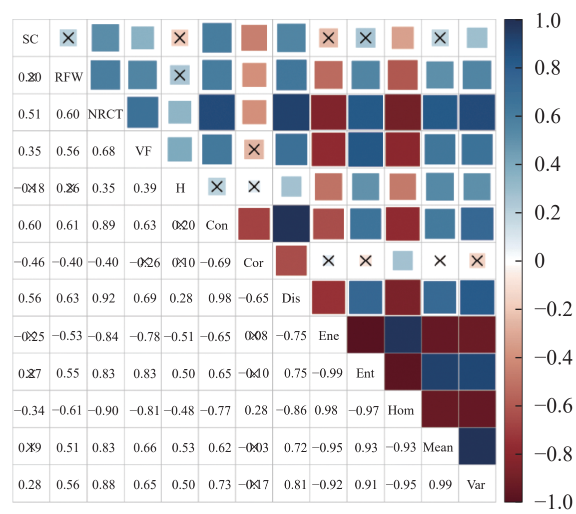

Fig. 6 Correlation analysis of RGB structure and texture parameters.

Among the five spectral reflectance bands and twelve vegetation indices, sugar content has no correlation with the reg band reflectance, but shows significant correlation with most of the spectral vegetation indices. Sugar content is positively correlated with the reflectance of green and blue bands, as well as GRVI, PPR, and TO. Conversely, sugar content is negatively correlated with the reflectance of the NIR band and other spectral vegetation indices, with the range of $|r|$ varying from 0.40 to 0.60. The correlation coefficients between the characteristic variables extracted by multispectral data and sugar content are higher than those with root fresh weight based on the heatmap (Fig. 7). There is multicollinearity between the different characteristic parameters. The specific variable screening results can be found in Table 5.

By comparing their importance with that of shadow characteristics, the Boruta algorithm selects a set of characteristics that minimizes the loss function for sugar content and root fresh weight prediction models as shown in Table 6. Fig. 8 shows the characteristic variable results for sugar content and root fresh weight based on the Boruta algorithm. For sugar content, the Boruta algorithm ultimately selects 8 characteristic variables based on the RGB sensor, 11 characteristic variables based on the multispectral sensor, and 15 parameters based on the combined multispectral and RGB sensors. Compared with the RGB sensor, the multispectral sensor may be more helpful in predicting sugar content. For root fresh weight, the Boruta algorithm ultimately selects 13 characteristic variables based on the RGB sensor, 10 characteristic variables based on the multispectral sensor, and 16 parameters based on the combined multispectral and RGB sensors. The top 7 characteristic parameters in terms of importance score for root fresh weight, including Hom, NGBDI, Dis, Con, VARI, Ent, and Ene, are all RGB characteristic parameters. For root fresh weight, the RGB sensor may be relatively advantageous compared with the multispectral sensor.

B. Sugar Content Modeling and Accuracy Evaluation

Based on the characteristic variables screened by the Boruta algorithm, the test set results of the three machine learning sugar content prediction models constructed are shown in Figs. 9–11. Each modeling method corresponds to six data types: RGB parameters, multispectral parameters, RGB and multispectral combined parameters, RGB and thermal infrared combined parameters, multispectral and thermal infrared combined parameters, and RGB, multispectral, and thermal infrared combined parameters, as shown in Table 7. Three machine learning algorithms are feasible to estimate the sugar content. The estimation effect of 94 days after sowing is closer to the 1:1 line, which is generally better than the estimation effect of 72 days and 86 days after sowing.

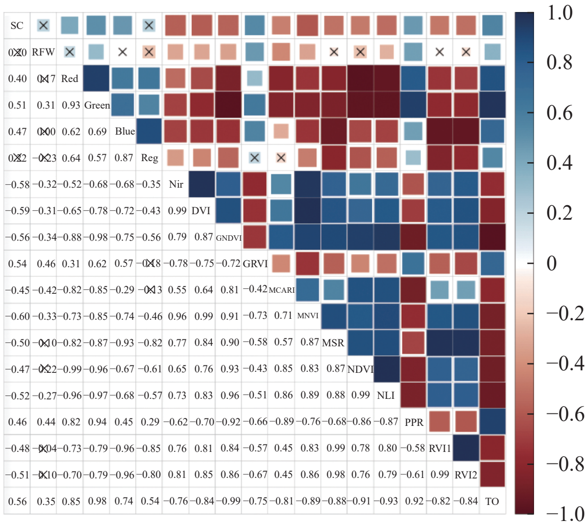

Fig. 7 Correlation analysis of multispectral vegetation indices.

For the estimation accuracy of the sugar content, the RF and PLS methods are better than the SVM model, as shown in Table 7. The optimal estimation of sugar content is based on the combined multispectral and thermal infrared parameters and PLS model, which achieves an R^2 of 0.61 and an rRMSE of 8.03%. In terms of sugar content, the multispectral parameters are more accurate than the RGB parameters when obtained from a single sensor, particularly the RF and PLS modelling methods are used. The prediction accuracy of the combined multi-sensor feature parameters for sugar content is generally better than that of the single sensor parameter. The introduction of thermal infrared parameters improves the model accuracy, with rRMSE decreasing by more than 0.6%. In addition, canopy thermal information adds some complementary information to the spectral characteristics in the prediction of sugar content.

Table 5 Different sensor drone characteristic variables associated with sugar content and root fresh weight at $\alpha = 0.01$ significance level.

Result	Sensor	Characteristic variables
Sugar content	RGB	VF, Con, Dis, GLI, NGBDI, RGBVI, VEG, Cor, Hom
	MS	Green, Blue, GRVI, PPR, TO, NIR, DVI, GNDVI, MCARI, MNVI, MSR, NDVI, NLI, RVI1, RVI2
Root fresh weight	RGB	Green, VARI, WI, VF, Con, Dis, Ent, Mean, Var, Red, Blue, GLI, NGBDI, RGBVI, VEG, Cor, Ene, Hom
	MS	Green, GRVI, PPR, TO, NIR, DVI, GNDVI, MCARI, MNVI, NLI

Table 6 Characteristic variables for sugar content and fresh weight of roots screened based on Boruta algorithm.

Result	Sensor	Characteristic variables
Sugar content	RGB	VF, Cor, Con, Dis, GLI, NGBDI, RGBVI, VEG
	MS	Green, Blue, NIR, GRVI, TO, DVI, GNDVI, MNVI, MSR, NLI, RVI2
	RGB + MS	VF, Con, Dis, NGBDI, RGBVI, Green, Blue, NIR, GRVI, TO, DVI, GNDVI, MNVI, NLI, RVI2
Root fresh weight	RGB	VF, Con, Cor, Dis, Ent, Ene, Hom, Green, Blue, VARI, WI, NGBDI, RGBVI
	MS	Green, NIR, GRVI, PPR, TO, DVI, GNDVI, MCARI, MNVI, NLI
	RGB + MS	VF, Con, Cor, Dis, Ent, Ene, Hom, Blue, VARI, WI, NGBDI, RGBVI, PPR, MCARI, MNVI, NLI

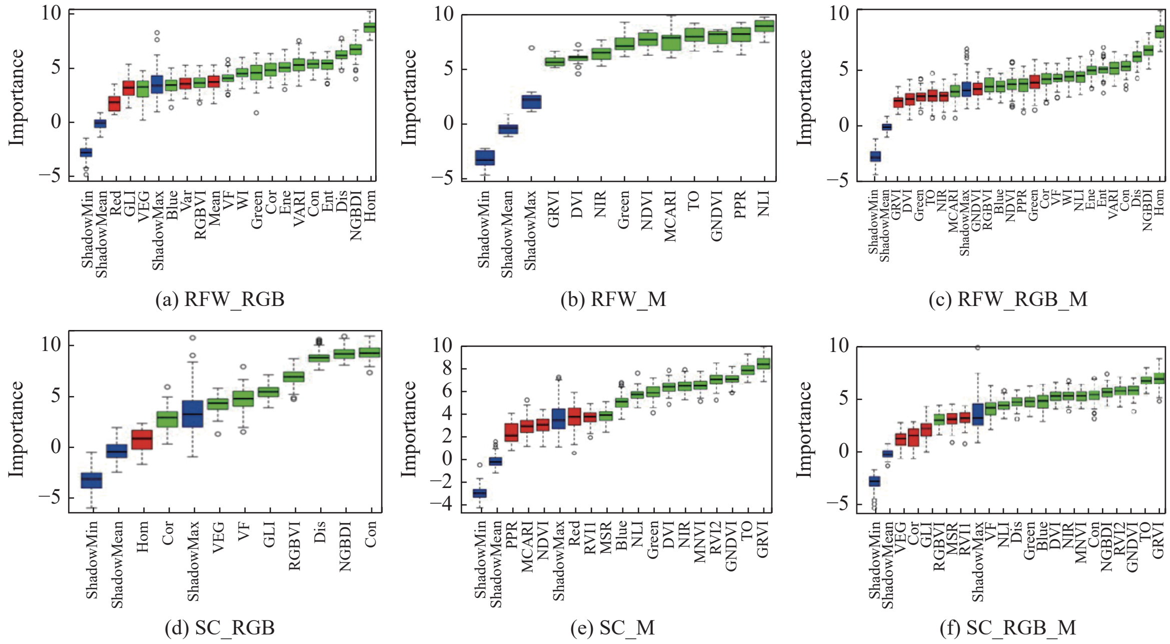

Fig. 8 Secondary characteristic screening of Boruta algorithm for fresh weight and sugar content. Root fresh weight and sugar content based on ((a) and (d)) RGB sensor, ((b) and (e)) multispectral sensor, and ((c) and (f)) RGB and multispectral sensor. The three blue boxes correspond to the minimum, average, and maximum values of the shadow characteristic importance score from low to high. The green boxes correspond to the characteristics that are accepted for the importance score assessment. The red boxes correspond to the rejected characteristics.

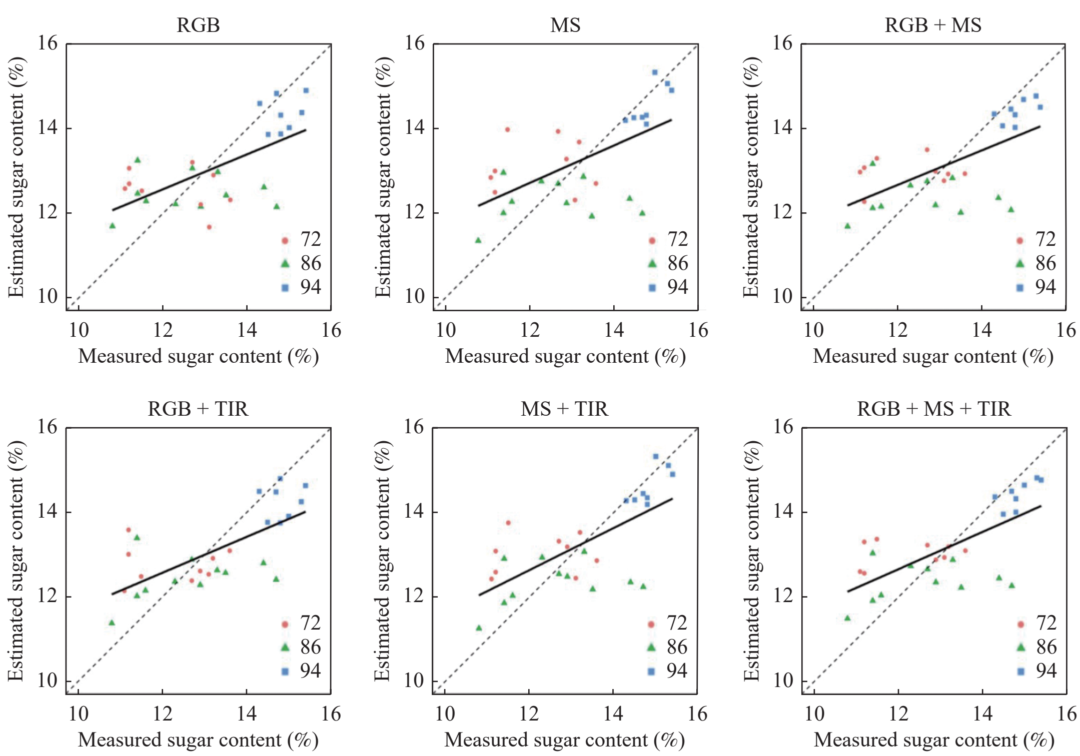

Fig. 9 Comparison of estimated and measured sugar contents based on RF method. RGB, MS, and TIR represent the characteristic parameters constructed based on RGB, multispectral, and thermal infrared sensors, respectively. The days after sowing are 72, 86, and 94.

C. Root Fresh Modelling and Accuracy Assessment

The SVM modelling accuracy is higher than RF and PLS in the root fresh weight models as shown in Table 8. For single sensor feature parameters, the modeling accuracy of feature parameters extracted based on the RGB is higher than that of based on the multispectral parameters. Compared with the single RGB parameter, the accuracy of both RF and PLS models constructed by combining RGB parameters with other sensor parameters decreases. The introduction of thermal infrared parameters has no significant effect on the accuracy of constructed RF and PLS models. For the SVM models, the

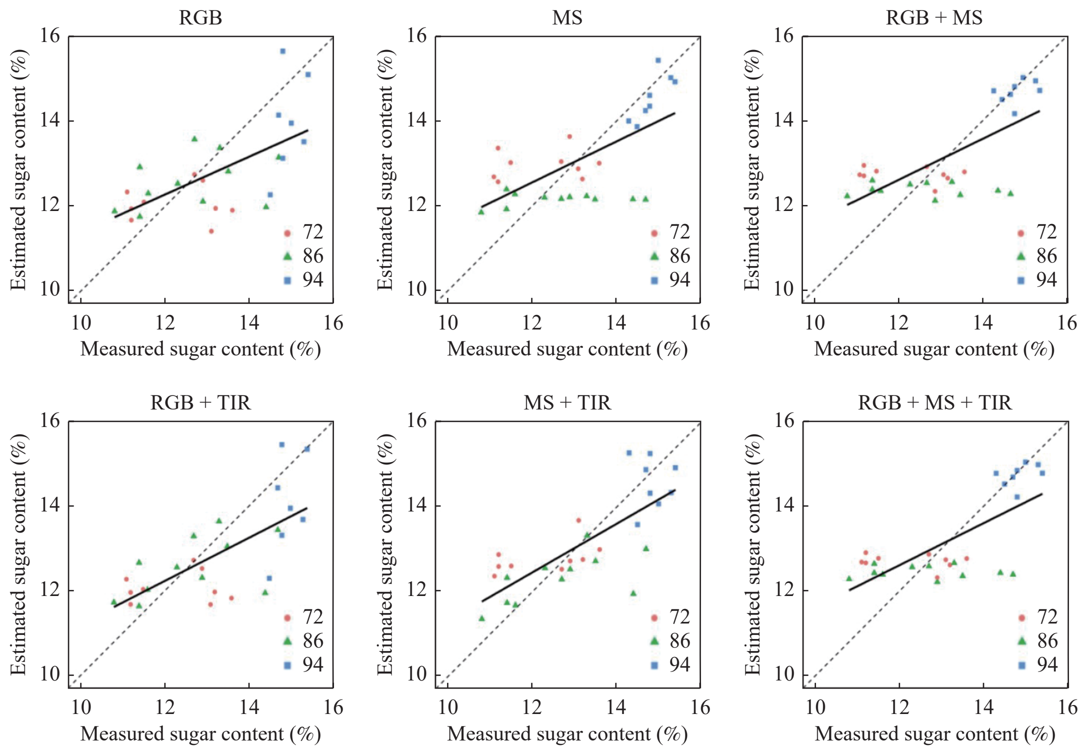

Fig. 10 Comparison of estimated and measured sugar contents based on PLS method.

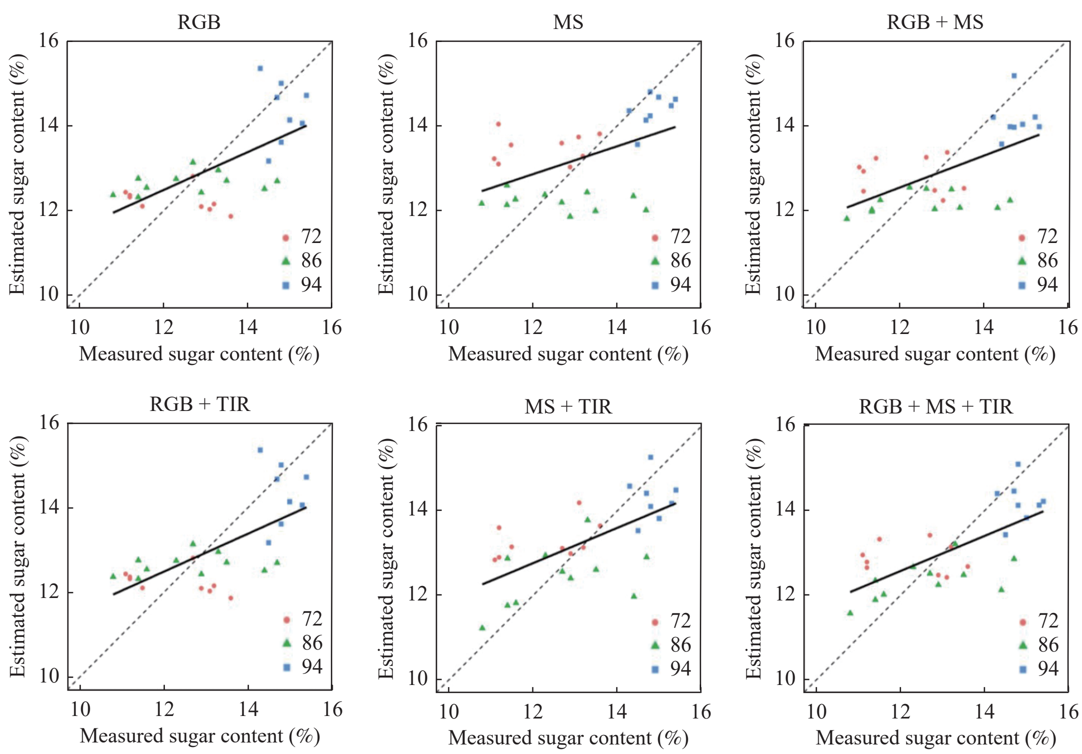

Fig. 11 Comparison of estimated and measured sugar contents based on SVM method.

accuracy is improved for both RGB and multispectral parameters combined with thermal infrared parameters respectively, compared with the single parameter modelling. When RGB, multispectral, and TIR parameters are modelled combinedly, the model accuracy decreases relative to the various parameter modeling combinations.

D. Field Modelling and Accuracy Assessment

Since yield and tubers fresh weight are closely related, it is clear that good prediction results can be achieved by modelling with a single RGB parameter. Therefore, a yield estimation model is constructed based on the screened RGB characteristic parameters. Because of the less gradient range of single-period data in the harvest period compared with

Table 7 Comparing estimation accuracy of sugar content model.

Algorithm	Method	R^2	RMSE (%)	rRMSE (%)
RF	RGB	0.39	1.30	9.86
	MS	0.47	1.22	9.24
	RGB + MS	0.51	1.19	9.01
	RGB + TIR	0.46	1.20	9.13
	MS + TIR	**0.57**	**1.10**	**8.37**
	RGB + MS + TIR	0.59	1.11	8.41
PLS	RGB	0.34	1.39	10.54
	MS	0.49	1.19	9.04
	RGB + MS	0.47	1.23	9.32
	RGB + TIR	0.39	1.33	10.09
	MS + TIR	**0.61**	**1.06**	**8.03**
	RGB + MS + TIR	0.49	1.20	9.12
SVM	RGB	0.42	1.27	9.72
	MS	0.30	1.40	10.63
	RGB + MS	0.42	1.28	9.76
	RGB + TIR	0.42	1.28	9.73
	MS + TIR	0.48	1.22	9.27
	RGB + MS + TIR	**0.51**	**1.20**	**9.10**

Note: RGB, MS, and TIR represent modelling based on characteristic parameters constructed from RGB, multispectral, and thermal infrared sensors, respectively. Bold numbers are the highest estimation accuracy under the same machine learning method.

Table 8 Comparing estimation accuracy of root fresh weight model.

Algorithm	Method	R^2	RMSE (%)	rRMSE (%)
RF	RGB	**0.47**	**84.6**	**26.6**
	MS	0.48	91.8	28.8
	RGB + MS	0.48	85.9	27.0
	RGB + TIR	0.42	88.8	27.9
	MS + TIR	0.48	92.0	28.9
	RGB + MS + TIR	0.50	85.6	26.9
PLS	RGB	**0.56**	**80.8**	**25.4**
	MS	0.35	95.6	30.1
	RGB + MS	0.54	82.0	25.8
	RGB + TIR	0.56	80.9	25.4
	MS + TIR	0.29	101.2	31.8
	RGB + MS + TIR	0.55	81.9	25.7
SVM	RGB	0.53	79.4	24.9
	MS	0.52	80.4	25.3
	RGB + MS	0.43	86.8	27.3
	RGB + TIR	0.54	78.6	24.7
	MS + TIR	**0.58**	**75.3**	**23.7**
	RGB + MS + TIR	0.43	87.3	27.5

Note: RGB, MS, and TIR represent modelling based on characteristic parameters constructed from RGB, multispectral, and thermal infrared sensors, respectively. Bold numbers are the highest estimation accuracy under the same machine learning method.

multiple periods, R^2 is less informative as an evaluation index. Therefore, when the yield model is evaluated for accuracy, the evaluation index R^2 is excluded. The RF model has a higher accuracy than the PLS and SVM models in yield modelling. The accuracy of the RF and PLS yield models is higher at 72, 86, and 94 days after sowing, and the accuracy of the SVM model is the worst at 94 days after sowing relative to the other periods when modeling using single period characteristic parameters. The RF, PLS, and SVM yield prediction models all show the highest accuracy in modelling the combined period characteristics at 86 and 94 days after sowing. The accuracy of modeling is improved relative to the single period. Except for the combined period modelling at 86 and 94 days after sowing, the accuracy of RF and SVM yield models combined in all the other periods is reduced relative to the accuracy of RF and SVM modeling in single period.

IV. Discussion

Sugar beet is a major sugar crop in temperate regions. Accurate and rapid estimation of biomass-related traits during the sugar accumulation period is essential for the selection of superior varieties and the optimization of sugar beet production. Feature selection plays an important role in machine learning, because it helps identify variables that are informative for the target trait while removing redundant or uninformative predictors, thereby improving both the model interpretability and the predictive performance. Commonly used feature selection approaches include filter, wrapper, and embedded methods, each of which can be applied according to specific analytical objectives. Among these, Boruta, an embedded feature selection method, has shown strong performance in the assessment of several plant phenotypes, such as wheat yield and maize relative chlorophyll content.

Plant height is an important structural trait for evaluating crop growth and has often been used as an indicator of canopy development [49]. Previous studies have shown that canopy height, particularly when combined with visible and multispectral vegetation indices, can contribute to yield estimation. However, plant height was not retained during feature selection in the present study, which differed from the findings of Ref. [14]. This discrepancy is likely related to the growth characteristics of sugar beet. During the sugar accumulation period, plant height tends to increase more slowly and eventually stabilizes, which limits its sensitivity for trait estimation at this stage.

UAVs have become increasingly important for plot-scale acquisition of crop phenotypic traits in breeding and precision agriculture. UAVs offer greater flexibility, stronger timeliness, and higher spatial resolution than the satellite remote sensing, making them well suitable for field-based phenotyping. In this paper, rapid and non-destructive extraction of sugar beet phenotypic information is achieved using UAV-based RGB, thermal infrared, and multispectral imagery. Based on these data, sugar content, root fresh weight, and yield are estimated using machine learning methods. The results show that feature combinations derived from multiple sensors generally outperform those based on a single sensor, which is consistent with previous findings [50, 51]. This is likely because multimodal data provide more comprehensive and complementary information than single-source data alone, thereby improving model robustness and prediction accuracy through mutual support and correction among different sensor types [52, 53].

RF, PLS, and SVM are used to develop prediction models for sugar content and root fresh weight. For sugar content, model performance ranged from $R^2 = 0.30$ to 0.61, with rRMSE values between 8.03% and 10.63%. Previous studies have likewise shown that sugar beet traits can be effectively estimated using remotely sensed spectral information. For instance, Wang et al. [54] used Bayesian ridge regression (BRR) and PLSR to model structural and spectral features extracted from multi-stage RGB, multispectral, thermal infrared, hyperspectral, and LiDAR UAV imagery, achieving a sugar content prediction accuracy of $R^2 = 0.64$ and rRMSE $< 7.20\%$. Cao et al. [55] estimated root fresh weight using the wide dynamic range vegetation index and an improved NDVI, obtaining accuracies of $R^2 = 0.935$ and rRMSE = 20.60% and $R^2 = 0.928$ and rRMSE $= 21.70\%$, respectively. Compared with these studies, the relatively lower R^2 and higher rRMSE observed here may be explained by the inclusion of multiple sugar beet varieties and sampling during the sugar accumulation period, when the variation in root sugar content and fresh weight among varieties is relatively limited. Although this reduces the range of the target variables and thus lowers model accuracy, it likely improves the varietal adaptability of the developed models. Therefore, the proposed models may still provide a useful reference for predicting sugar content and root fresh weight across different sugar beet varieties.

With the rapid development of remote sensing technology, methods for estimating crop biomass and yield have become increasingly diverse. In the present studies, the RF model shows a slight advantage over PLS, which is consistent with previous reports on winter rapeseed biomass estimation [23] and potato yield prediction [8]. RF is well suited for nonlinear problems and is relatively resistant to overfitting [56]. By contrast, PLS is less effective for strongly nonlinear relationships and some information may be lost during dimensionality reduction. In the modelling of root fresh weight, SVM outperforms both RF and PLS, which agrees with the findings of Ref. [57] for soybean seed yield prediction using multimodal data fusion. The stronger performance of SVM in the present study may be attributed to its ability to handle nonlinear relationships in high-dimensional feature spaces, especially under relatively small sample sizes. Overall, all the three algorithms produce satisfactory results for modelling sugar content and root fresh weight in sugar beet.

Overall, this paper provides a useful technical approach for sugar beet phenotypic analysis and offers insights for precision agricultural management and variety selection. From a production perspective, integrating multi-sensor UAV observations with spatial field variability may further support management-oriented decision-making. For example, spatial predictions of yield and quality traits can be used to identify within-field heterogeneity, delineate management zones, support harvest planning, and prioritize fields or subplots with greater production potential or quality value. When combined with digital field records and operational planning, such information may also facilitate more targeted allocation of labor, machinery, and logistics during the harvest period.

However, the practical application of this paper at commercial scale still requires careful evaluation. Its utility depends not only on predictive performance, but also on the cost and accessibility of multi-sensor UAV platforms, the efficiency of image acquisition under field conditions, the complexity of data-processing workflows, and the extent to which the outputs can be integrated with existing agricultural machinery and farm management systems. In particular, the added value of combining RGB, multispectral, and thermal infrared sensors shall be weighed against the increased operational and economic costs associated with multi-sensor deployment. Therefore, future studies will move beyond model accuracy alone and further assess the operational feasibility, processing efficiency, and cost-effectiveness of this approach under the real production conditions. Such work will help to clarify its practical value for large-scale application in the commercial sugar beet production.

V. Conclusion

Ten high-quality commercial varieties of sugar beet suitable for high latitudes are selected for this paper. UAV platforms equipped with RGB, multispectral, and thermal infrared sensors are used to acquire field imagery at multiple time points. Phenotypic features, including canopy structural traits, textural characteristics, thermal indices, and vegetation indices, are extracted for each plot. Feature variables are then screened using correlation analysis and the Boruta algorithm. The three modelling methods, RF, PLS, and SVM, all provide satisfactory estimations of sugar content, root fresh weight, and yield in sugar beet. In general, sensor-derived combined feature sets achieve higher prediction accuracy for sugar content than single-sensor inputs. These findings demonstrate the potential of multi-sensor UAV data for dynamic monitoring of sugar beet growth and provide useful support for variety screening and precision production of commercial sugar beet under the high-latitude conditions.

Acknowledgment

This work was supported by the Industrial Technology Innovation Program of IMAST (No. 2024RCYJ04004) and the Inner Mongolia Science and Technology Supported Project (No. 2024CYCX04001).

References

[1] M. S. Hossain, A. I. ElSayed, M. Moore, and K. J. Dietz, Redox and reactive oxygen species network in acclimation for salinity tolerance in sugar beet, *J. Exp. Bot.*, 2017, 68(5), 1283–1298.

[2] J. C. Dohm, A. E. Minoche, D. Holtgräwe, S. Capella-Gutiérrez, F. Zakrzewski, H. Tafer, O. Rupp, T. R. Sörensen, R. Stracke, R. Reinhardt et al., The genome of the recently domesticated crop plant sugar beet (*Beta vulgaris*), *Nature*, 2014, 505(7484), 546–549.

[3] A. A. Sulaiman, Y. Sulaeman, N. Mustikasari, D. Nursyamsi, and A. M. Syakir, Increasing sugar production in Indonesia through land suitability analysis and sugar mill restructuring, *Land*, 2019, 8(4), 61.

[4] L. Malambo, S. C. Popescu, S. C. Murray, E. Putman, N. A. Pugh, D. W. Horne, G. Richardson, R. Sheridan, W. L. Rooney, R. Avant et al., Multitemporal field-based plant height estimation using 3D point clouds generated from small unmanned aerial systems high-resolution imagery, *Int. J. Appl. Earth Obs. Geoinf.*, 2018, 64, 31–42.

[5] J. Yue, H. Feng, Z. Li, C. Zhou, and K. Xu, Mapping winter-wheat biomass and grain yield based on a crop model and UAV remote sensing, *Int. J. Remote Sens.*, 2021, 42(5), 1577–1601.

[6] M. V. Ferro and P. Catania, Technologies and innovative methods for

precision viticulture: A comprehensive review, *Horticulturae*, 2023, 9(3), 399.

[7] X. Zhou, Y. Kono, A. Win, T. Matsui, and T. S. T. Tanaka, Predicting within-field variability in grain yield and protein content of winter wheat using UAV-based multispectral imagery and machine learning approaches, *Plant Prod Sci.*, 2021, 24(2), 137–151.

[8] B. Li, X. Xu, L. Zhang, J. Han, C. Bian, G. Li, J. Liu, and L. Jin, Above-ground biomass estimation and yield prediction in potato by using UAV-based RGB and hyperspectral imaging, *ISPRS J. Photogramm. Remote Sens.*, 2020, 162, 161–172.

[9] T. Wheeler and J. Von Braun, Climate change impacts on global food security, *Science*, 2013, 341(6145), 508–513.

[10] J. Verrelst, J. P. Rivera, F. Veroustraete, J. Muñoz-Marí, J. G. P. W. Clevers, G. Camps-Valls, and J. Moreno, Experimental Sentinel-2 LAI estimation using parametric, non-parametric and physical retrieval methods—A comparison, *ISPRS J. Photogramm. Remote Sens.*, 2015, 108, 260–272.

[11] B. Gano, S. Bhadra, J. M. Vilbig, N. Ahmed, V. Sagan, and N. Shakoor, Drone-based imaging sensors, techniques, and applications in plant phenotyping for crop breeding: A comprehensive review, *Plant Phenome J.*, 2024, 7(1), e20100.

[12] L. Feng, S. Chen, C. Zhang, Y. Zhang, and Y. He, A comprehensive review on recent applications of unmanned aerial vehicle remote sensing with various sensors for high-throughput plant phenotyping, *Comput. Electron. Agric.*, 2021, 182, 106033.

[13] O. Bongomin, J. Lamo, J. M. Guina, C. Okello, G. G. Ocen, M. Obura, S. Alibu, C. A. Owino, A. Akwero, and S. Ojok, UAV image acquisition and processing for high-throughput phenotyping in agricultural research and breeding programs, *Plant Phenome J.*, 2024, 7(1), e20096.

[14] J. Bendig, K. Yu, H. Aasen, A. Bolten, S. Bennertz, J. Broscheit, M. L. Gnyp, and G. Bareth, Combining UAV-based plant height from crop surface models, visible, and near infrared vegetation indices for biomass monitoring in barley, *Int. J. Appl. Earth Obs. Geoinf.*, 2015, 39, 79–87.

[15] F. Gnädinger and U. Schmidhalter, Digital counts of maize plants by unmanned aerial vehicles (UAVs), *Remote Sens.*, 2017, 9(6), 544.

[16] X. Jin, S. Liu, F. Baret, M. Hemerlé, and A. Comar, Estimates of plant density of wheat crops at emergence from very low altitude UAV imagery, *Remote Sens. Environ.*, 2017, 198, 105–114.

[17] R. Ballesteros, J. F. Ortega, D. Hernandez, and M. A. Moreno, Onion biomass monitoring using UAV-based RGB imaging, *Precis. Agric.*, 2018, 19(5), 840–857.

[18] A. J. Mathews and J. L. R. Jensen, Visualizing and quantifying vineyard canopy LAI using an unmanned aerial vehicle (UAV) collected high density structure from motion point cloud, *Remote Sens.*, 2013, 5(5), 2164–2183.

[19] T. Duan, B. Zheng, W. Guo, S. Ninomiya, Y. Guo, and S. C. Chapman, Comparison of ground cover estimates from experiment plots in cotton, sorghum and sugarcane based on images and ortho-mosaics captured by UAV, *Funct. Plant Biol.*, 2016, 44(1), 169–183.

[20] S. Xu, X. Xu, C. Blacker, R. Gaulton, Q. Zhu, M. Yang, G. Yang, J. Zhang, Y. Yang, M. Yang et al., Estimation of leaf nitrogen content in rice using vegetation indices and feature variable optimization with information fusion of multiple-sensor images from UAV, *Remote Sens.*, 2023, 15(3), 854.

[21] H. Croft, J. M. Chen, Y. Zhang, A. Simic, T. L. Noland, N. Nesbitt, and J. Arabian, Evaluating leaf chlorophyll content prediction from multispectral remote sensing data within a physically-based modelling framework, *ISPRS J. Photogramm. Remote Sens.*, 2015, 102, 85–95.

[22] N. Okole, F. R. I. Yamati, R. Hossain, M. Varrelmann, A. K. Mahlein, and R. H. J. Heim, Aerial low-altitude remote sensing and deep learning for in-field disease incidence scoring of virus yellows in sugar beet, *Plant Pathol.*, 2024, 73(9), 2310–2324.

[23] Y. Liu, S. Liu, J. Li, X. Guo, S. Wang, and J. Lu, Estimating biomass of winter oilseed rape using vegetation indices and texture metrics derived from UAV multispectral images, *Comput. Electron. Agric.*, 2019, 166, 105026.

[24] H. S. Ndlovu, J. Odindi, M. Sibanda, and O. Mutanga, A systematic review on the application of UAV-based thermal remote sensing for assessing and monitoring crop water status in crop farming systems, *Int. J. Remote Sens.*, 2024, 45(15), 4923–4960.

[25] S. W. Shivers, D. A. Roberts, and J. P. McFadden, Using paired thermal and hyperspectral aerial imagery to quantify land surface temperature variability and assess crop stress within California orchards, *Remote Sens. Environ.*, 2019, 222, 215–231.

[26] T. Liu, R. Li, X. Zhong, M. Jiang, X. Jin, P. Zhou, S. Liu, C. Sun, and W. Guo, Estimates of rice lodging using indices derived from UAV visible and thermal infrared images, *Agric. For. Meteor.*, 2018, 252, 144–154.

[27] M. Maimaitijiang, A. Ghulam, P. Sidike, S. Hartling, M. Maimaitiyiming, K. Peterson, E. Shavers, J. Fishman, J. Peterson, S. Kadam et al., Unmanned aerial system (UAS)-based phenotyping of soybean using multi-sensor data fusion and extreme learning machine, *ISPRS J. Photogramm. Remote Sens.*, 2017, 134, 43–58.

[28] M. Khoshboresh-Masouleh, F. Alidoost, and H. Arefi, Multiscale building segmentation based on deep learning for remote sensing RGB images from different sensors, *J. Appl. Remote Sens.*, 2020, 14(3), 034503.

[29] Q. Wang, Y. Che, K. Shao, J. Zhu, R. Wang, Y. Sui, Y. Guo, B. Li, L. Meng, and Y. Ma, Estimation of sugar content in sugar beet root based on UAV multi-sensor data, *Comput. Electron. Agric.*, 2022, 203, 107433.

[30] G. E. Meyer and J. C. Neto, Verification of color vegetation indices for automated crop imaging applications, *Comput. Electron. Agric.*, 2008, 63(2), 282–293.

[31] D. M. Woebbecke, G. E. Meyer, K. Von Bargen, and D. A. Mortensen, Color indices for weed identification under various soil, residue, and lighting conditions, *Trans. ASAE*, 1995, 38(1), 259–269.

[32] M. Louhaichi, M. M. Borman, and D. E. Johnson, Spatially located platform and aerial photography for documentation of grazing impacts on wheat, *Geocarto Int.*, 2001, 16(1), 65–70.

[33] J. Verrelst, M. E. Schaepman, B. Koetz, and M. Kneubühler, Angular sensitivity analysis of vegetation indices derived from CHRIS/PROBA data, *Remote Sens. Environ.*, 2008, 112(5), 2341–2353.

[34] A. A. Gitelson, Y. J. Kaufman, R. Stark, and D. Rundquist, Novel algorithms for remote estimation of vegetation fraction, *Remote Sens. Environ.*, 2002, 80(1), 76–87.

[35] C. J. Tucker, Red and photographic infrared linear combinations for monitoring vegetation, *Remote Sens. Environ.*, 1979, 8(2), 127–150.

[36] A. A. Gitelson and M. N. Merzlyak, Remote sensing of chlorophyll concentration in higher plant leaves, *Adv. Space Res.*, 1998, 22(5), 689–692.

[37] T. Hague, N. D. Tillett, and H. Wheeler, Automated crop and weed monitoring in widely spaced cereals, *Precis. Agric.*, 2006, 7(1), 21–32.

[38] C. S. T. Daughtry, C. L. Walthall, M. S. Kim, E. B. de Colstoun, and J. E. McMurtrey III, Estimating corn leaf chlorophyll concentration from leaf and canopy reflectance, *Remote Sens. Environ.*, 2000, 74(2), 229–239.

[39] P. Gong, R. Pu, G. S. Biging, and M. R. Larrieu, Estimation of forest leaf area index using vegetation indices derived from Hyperion hyperspectral data, *IEEE Trans. Geosci. Remote Sens.*, 2003, 41(6), 1355–1362.

[40] J. M. Chen, Evaluation of vegetation indices and a modified simple ratio for boreal applications, *Can. J. Remote Sens.*, 1996, 22(3), 229–242.

[41] J. W. Rouse, Monitoring the vernal advancement and retrogradation of natural vegetation, NASA/GSFCT Type II Report, NASA, Greenbelt, MD, USA, 1973.

[42] N. S. Goel and W. Qin, Influences of canopy architecture on relationships between various vegetation indices and LAI and FPAR: A computer simulation, *Remote Sens. Rev.*, 1994, 10(4), 309–347.

[43] G. Metternicht, Vegetation indices derived from high-resolution airborne videography for precision crop management, *Int. J. Remote Sens.*, 2003, 24(14), 2855–2877.

[44] R. L. Pearson and L. D. Miller, Remote mapping of standing crop biomass for estimation of the productivity of the short-grass prairie, in *Proc. 8th International Symposium on Remote Sensing of Environment*, Ann Arbor, MI, USA, 1972, 1357–1381.

[45] L. Xue, W. Cao, W. Luo, T. Dai, and Y. Zhu, Monitoring leaf nitrogen status in rice with canopy spectral reflectance, *Agron. J.*, 2004, 96(1), 135–142.

[46] N. H. Broge and E. Leblanc, Comparing prediction power and stability of broadband and hyperspectral vegetation indices for estimation of green leaf area index and canopy chlorophyll density, *Remote Sens. Environ.*, 2001, 76(2), 156–172.

[47] L. Breiman, Random forests, *Mach. Learn.*, 2001, 45(1), 5–32.

[48] M. B. Kursa and W. R. Rudnicki, Feature selection with the Boruta package, *J. Stat. Software*, 2010, 36(11), 1–13.

[49] D. J. Selkowitz, G. Green, B. Peterson, and B. Wylie, A multi-sensor Lidar, multi-spectral and multi-angular approach for mapping canopy height in boreal forest regions, *Remote Sens. Environ.*, 2012, 121, 458–471.

[50] S. Liu, X. Jin, C. Nie, S. Wang, X. Yu, M. Cheng, M. Shao, Z. Wang, N. Tuohuti, Y. Bai et al., Estimating leaf area index using unmanned aerial vehicle data: Shallow vs. deep machine learning algorithms, *Plant Physiol.*, 2021, 187(3), 1551–1576.

[51] D. Lahat, T. Adali, and C. Jutten, Multimodal data fusion: An overview of methods, challenges, and prospects, *Proc. IEEE*, 2015, 103(9), 1449–1477.

[52] F. Samadzadegan, A. Toosi, and F. Dadrass Javan, A critical review on multi-sensor and multi-platform remote sensing data fusion approaches: Current status and prospects, *Int. J. Remote Sens.*, 2025, 46(3), 1327–1402.

[53] S. Salcedo-Sanz, P. Ghamisi, M. Piles, M. Werner, L. Cuadra, A. Moreno-Martínez, E. Izquierdo-Verdiguier, J. Muñoz-Marí, A. Mosavi, and G. Camps-Valls, Machine learning information fusion in Earth observation: A comprehensive review of methods, applications and data sources, *Inf. Fusion*, 2020, 63, 256–272.

[54] N. Wang, J. G. P. W. Clevers, S. Wieneke, H. Bartholomeus, and L. Kooistra, Potential of UAV-based sun-induced chlorophyll fluorescence to detect water stress in sugar beet, *Agric. For. Meteor.*, 2022, 323, 109033.

[55] Y. Cao, G. L. Li, Y. K. Luo, Q. Pan, and S. Y. Zhang, Monitoring of sugar beet growth indicators using wide-dynamic-range vegetation index (WDRVI) derived from UAV multispectral images, *Comput. Electron. Agric.*, 2020, 171, 105331.

[56] W. Y. Loh, Classification and regression trees, *WIREs Data Min. Knowl. Discov.*, 2011, 1(1), 14–23.

[57] M. Maimaitijiang, V. Sagan, P. Sidike, S. Hartling, F. Esposito, and F. B. Fritschi, Soybean yield prediction from UAV using multimodal data fusion and deep learning, *Remote Sens. Environ.*, 2020, 237, 111599.

Yeying Zhou received the ME degree from China Agricultural University, Beijing, China, in 2022. She is currently pursuing the PhD degree at Inner Mongolia Academy of Science and Technology, China. Her research interests include remote sensing, crop model, and crop nitrogen management.

Yuntao Ma received the PhD degree in soil science from College of Resources and Environmental Sciences, China Agricultural University, Beijing, China, in 2006. From 2007 to 2009, she was a post-doctoral researcher at Institute of Automation, Chinese Academy of Sciences, China. She is currently a professor at China Agricultural University, China. Her research interests include plant 3D modeling and digital twins, machine-vision-based data mining for plant growth information, artificial intelligence and smart agriculture, UAV-enabled high-throughput phenotyping, and multi-source sensor development and applications in digital agriculture.